Full Length Research Article

© 2025, Centre for Advanced Research in Agricultural Sciences
Research Journal of Agricultural Sciences
Volume 16; Issue 05 (Sept–Oct 2025); pp 438–446

ISSN: 0976-1675 (P)
ISSN: 2249-4538 (E)

Green Synthesis, Characterization and Anticancer Activity of *Clerodendrum infortunatum* Mediated Ag Doped Y_2O_3 Nanoparticles

H. R. Uma[1, 3] and Jessica Fernando*[2, 3]

[1] Research Scholar (Register No: 20113112032013) Department of Chemistry, V. O. Chidambaram College, Thoothukudi - 628 008, Tamil Nadu, India
[2] Associate Professor, Department of Chemistry, V. O. Chidambaram College, Thoothukudi - 628 008, Tamil Nadu, India
[3] Affiliated to Manonmaniam Sundaranar University, Abishekapatti - 627 012, Tamil Nadu, India

Received: 20 Jul 2025; Revised accepted: 04 Sept 2025

Abstract

Over the years, the continuously increasing incidence rates of cancer and infectious diseases are open threats to the sustainable survival of animals and humans. In the last two decades, the demands of nanomaterials as modern therapeutic agents have increased. In this study, green fabrication of Ag doped Y_2O_3 nanoparticles using aqueous extract of *Clerodendrum infortunatum* as bio-reductant and assesses its potential as anticancer agent. The obtained pure Y_2O_3 and Ag doped Y_2O_3 were characterized by various analytical techniques including XRD, EDS, XPS, UV-visible and PL. The Ag doped Y_2O_3 nanoparticles was endured defect emissions that are more intense than those of pure samples, according to the obtained PL spectra. In addition to these fascinating findings, the samples deactivate against a AGS (Human gastric adenocarcinoma) cell line through an MTT trial, which highlighted the superiority of the doped when compared to the native nanoparticles. As a consequence, the Ag doped Y_2O_3 nanoparticles could potentially be an effective alternative for anticancer materials, particularly in biomedical applications.

***Key words*:** Green synthesis, Nanoparticles *Clerodendrum infortunatum* leaves, Anticancer activity, Cell viability

In recent years, with the development of nanotechnology, the use of various metal nanoparticles has become widespread specifically in the treatment of cancer. Gastric cancer is the fourth most common malignant tumor in the world and the incidence rate is higher in the developing countries compared to the developed countries [1]. Gastric cancer patients are usually diagnosed at the late stages. Combinational chemotherapy, radiotherapy, and surgery are used to treat patients with different stages of gastric cancer; however, the 5-year survival rate is low [2-3]. Further research is needed and appropriate research tools are required to develop novel therapeutic approaches. Many antibiotics with short half-lives must be administered often in traditional formulations in order to sustain anticancer action. Moreover, Yttrium oxide (Y_2O_3), a widespread rare earth metal, is significant for future use due to its thermal stability and chemical and mechanical reliability. Yttrium oxide is used in biomedical images, materials science, synthesis of inorganic compounds, optics, electricity, biology applications [4-8], and photodynamic therapy. Furthermore, the properties of Yttrium oxide can be modified by doping the transition metals such as Er, Eu, La, Yb and Ag to tune the properties of the nanomaterials [8-13]. Amid these transition metals, the doping of Ag is more important because this enhances the optical properties of Yttrium oxide nanomaterials [14]. Silver belongs to transition metal group with high thermal and electrical conductivity. The utilization of silver in medical and therapeutics is very old; however, basic antimicrobial behaviour is discovered later. In recent years silver NPs have achieved much attention in medical filed due to its various applications such as antimicrobial and anticancer [14]. In this respect, Y_2O_3 nanoparticles of different sizes and morphologies were developed through various methods, such as sonochemical, solvothermal, hydrothermal, electrochemical, sol-gel, and thermal decomposition [6-8]. However, most of these approaches include costly and toxic chemicals as stabilizing or capping agents; their environmental applications are limited. Interestingly, a promising method to overcome these limitations was developed that involves the utilization of plant extracts. In this present era, the biosynthesis of nanoparticles has been proposed as a cost-effective and environmentally friendly alternative to chemical and physical methods. Plant-mediated synthesis of nanoparticles is a green chemistry approach that connects nanotechnology with plants [15]. However, the green synthesize technique of nanostructure provides an eco-friendly solution for agricultural biomedical, and polluted environment remediation [16]. The synthesize technique of nanostructure and the any part of plant (peels, leaves, flowers, roots, seeds and stems) material contain secondary metabolites [17]. The secondary metabolites present in the extract of the leaf act as stabilizing and reducing agents to change metal ions into metal oxide nanoparticles. Kumar *et al*. [18] reported the phyto-mediated preparation of zinc oxide nanoparticles from *Clerodendrum infortunatum* L. leaf extract and find out the enhanced antibacterial potential. In fact, to

***Correspondence to:** Jessica Fernando, E-mail: jessivoc@yahoo.com

Citation: Uma HR, Fernando J. 2025. Green synthesis, characterization and anticancer activity of *Clerodendrum infortunatum* mediated Ag doped Y_2O_3 nanoparticles. *Res. Jr. Agril. Sci.* 16(5): 438-446.

date, no report of doping of elements within Y_2O_3 using *Clerodendrum infortunatum* L. leaf extract has been made, to the best of our knowledge. In this paper we report, undoped Y_2O_3 and Ag doped Y_2O_3 nanoparticles were prepared by green method using *Clerodendrum infortunatum* leaf extract and the obtained product were characterized with the support of XRD, TEM, EDS, XPS, UV–Visible and PL. The anticancer activity of nanoparticles was investigated using MTT assays.

MATERIALS AND METHODS

The chemical reagents used in this work were yttrium nitrate, silver nitrate ($AgNO_3$) which are attained from SRL Chemicals with 99% of purity and the entire reagents utilized were of analytical grade and used without further purification. All aqueous solutions were prepared using double distilled water.

Preparation of leaf extract

Clerodendrum infortunatum leaves were collected and cleaned with tap water followed by double distilled water repeatedly and dried. 30 g of leaves were mixed with 150 mL of double distilled water and boiled at 80 °C. During the process, a yellow-coloured solution was formed. Then the prepared extract was allowed to cool at room temperature and finally, it was filtered using Whatman filter paper and stored in a refrigerator for further purpose.

Synthesis of pure Y_2O_3 nanoparticles

5 g of yttrium nitrate was dissolved in 50 ml of double-distilled water. Then 10 ml of leaf extract is added to the solution with constant stirring, and sodium hydroxide was added to the above solution to adjust the pH to 9. The solution was kept on the magnetic stirrer for 2 hours. The precipitate was formed. The solution was undisturbed for 24 hours to settle the precipitate. The obtained precipitate is filtered and washed using double-distilled water and ethanol simultaneously and dried and muffled at 500 °C at 2hours for further characterizations.

Synthesis of silver doped Y_2O_3 nanoparticles

5g of yttrium nitrate and 0.5 g of $AgNO_3$ were dissolved with 50 ml of double-distilled water. Then 10 ml of leaf extract is added to the solution with constant stirring and sodium hydroxide was added to the above solution to adjust the pH to 9. The solution was kept on the magnetic stirrer for 2 hours. The precipitate was formed. The solution was undisturbed for 24 hours to settle the precipitate. The obtained precipitate is filtered and washed using double distilled water and ethanol simultaneously and dried and muffled at 500 °C at 2 hours for further characterizations.

Characterization section

The crystal structure, determination of phases and average crystallite size of synthesized samples were investigated by XRD (PANalytical X'Pert Pro, $\lambda = 1.5406$ Å, 40 kV and 30 mA) with Cu-K_α radiation. The transmission electron microscope (TEM, JEOL-JEM-2100F with an accelerating voltage of 200 kV) was used to create the nanoparticles micrographs. The X-ray Photoelectron Spectroscopic (XPS) measurement was undertaken by employing Photoelectron spectrometer (PHI 5000 Versa Probe 111) equipped with a high performance 0–5 keV Ar^+ ion gun and optional 10 and 20 kV C_{60} ion guns for the analysis of Y 3d, O 1s and Ag 3d peaks. To assess the samples The UV – Visible spectrum of synthesized samples were carried out UV absorbance Spectrophotometer (Perkin Elmer LAMBDA – 35) was employed at room temperature. Using a Cary Eclipse Photoluminescence Spectrophotometer at room temperature, the PL spectra of the samples were collected.

Anticancer activity

AGS (Human gastric adenocarcinoma) cell line was procured from NCCS, Pune, India. The cells were maintained in DMEM/F12 medium supplemented with 10 % FBS along with the 1% antibiotic-antimycotic solution in the atmosphere of 5% CO_2, 18-20% O_2 at 37^0C temperature in the CO_2 incubator and sub-cultured after 2 days. Passage number of AGS cells was 37 used for the current study. Seed 200 µl cell suspension in a 96-well plate at the required cell density (10,000 cells per well) and allow the cells to grow for about 24 hours. Add appropriate concentrations of the given test compounds which was diluted in complete media. Incubate the plate for 24hrs at 37 °C in a 5 % CO_2 atmosphere. After the incubation period, takeout the plates from incubator, and remove spent media and add MTT reagent to a final concentration of 0.5mg/ml of total volume. Wrap the plate with aluminium foil to avoid exposure to light. Return the plates to the incubator and incubate for 3 hours. Incubation time varies for different cell lines. Within one experiment, incubation time should be kept constant while making comparisons. Remove the MTT reagent and then add 100 µl of solubilisation solution (DMSO). Gentle stirring in a gyratory shaker will enhance dissolution. Occasionally, pipetting up and down may be required to completely dissolve the MTT formazan crystals especially in dense cultures. Read the absorbance on a spectrophotometer or an ELISA reader at 570 nm wavelength. The following formula was put into effect to record the percentage of cell viability.

$$\text{Cell viability (\%)} = \frac{\text{OD sample mean}}{\text{OD control mean}} \times 100\ \%$$

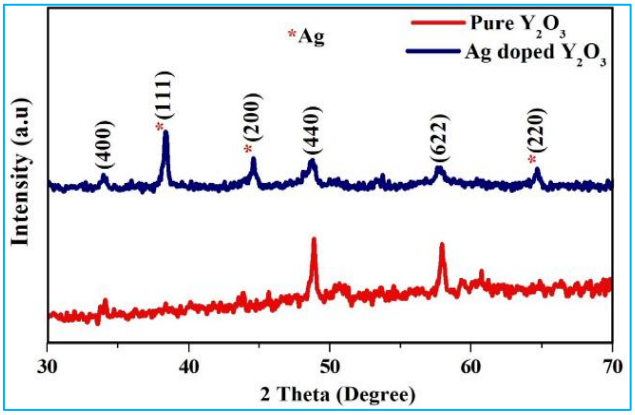

Fig 1 XRD spectra of pure Y_2O_3 and Ag doped Y_2O_3 nanoparticles

RESULTS AND DISCUSSION

XRD analysis

The X-ray diffraction pattern of nanoparticles (Fig 1) showed sharp reflections with respect to face cantered cubic (FCC) peaks obtained from XRD analysis were indicative of smaller size of nanoparticles. The assigned 2θ values for pure Y_2O_3 with respect to (400), (440) and (622) planes were 33.12°, 48.42° and 57.64° respectively and for Ag with respect to (111), (200) and (220) planes were 38.31°, 44.34° and 64.47° respectively. The XRD patterns for Y_2O_3 and Ag doped Y_2O_3 were in good agreement with the data available in JCPDS file no. 65-3178 and JCDPS file no 04-0783 respectively [19]. By examining the peak width as a function of diffracting angle 2θ,

Williamson-Hall (W-H)) method of deconvoluting size and strain broadening could produce the following mathematical expression [20]:

$$\beta \cos\theta = \varepsilon\,(4\sin\theta) + \left(\frac{K\lambda}{D}\right) \quad \text{---------- (1)}$$

where λ (1.5406 Å) is the x-ray wavelength, ε is the average microstrain, θ is the Bragg diffraction angle, k is the shape factor (0.94), and β is the full width at half-maximum in radians. For the synthesized nanoparticles, a plot is created with 4 sin θ along the x-axis and β cos θ along the y-axis. (Fig 2) displays the lattice strain for pure Y_2O_3 and Ag doped Y_2O_3 nanoparticles that have been determined from the slope of the W-H plot. According to the W-H method's findings, the pure Y_2O_3 and Ag doped Y_2O_3 crystallite sizes are around 25.14 nm and 16.21 nm, respectively.

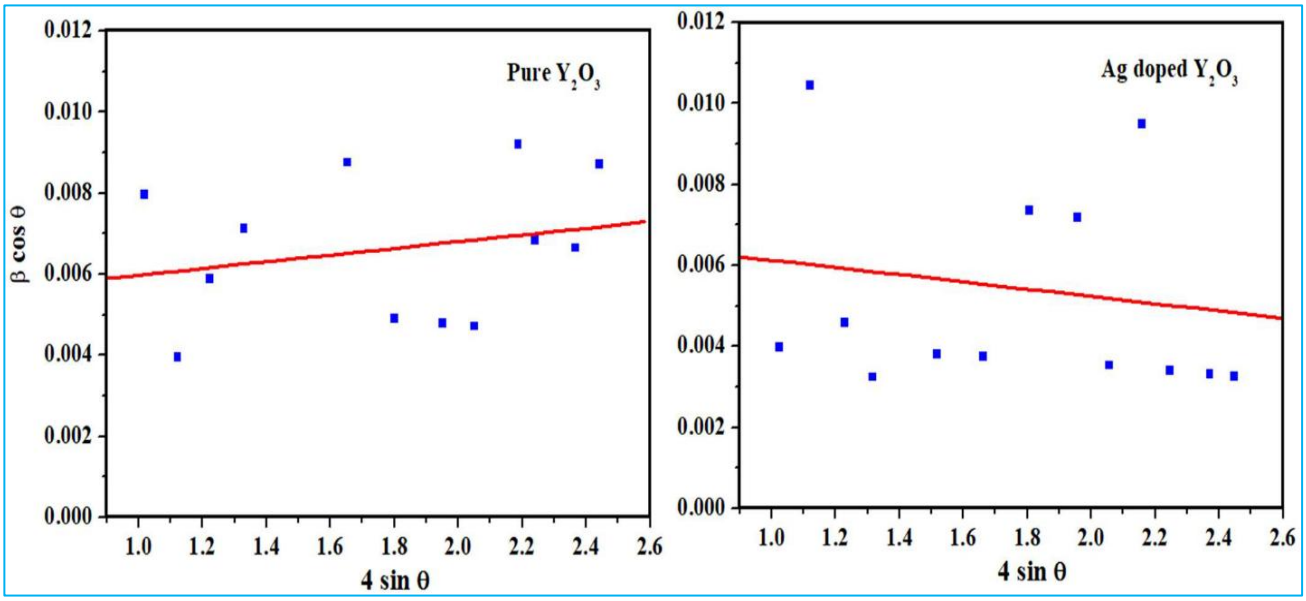

Fig 2 W-H plot for pure Y_2O_3 and Ag doped Y_2O_3 nanoparticles

The values of particle size, strain and dislocation density have been calculated and tabulated in (Table 1). From the table, the obtained values of dislocation density (δ) are for Ag doped Y_2O_3 ($.81 \times 10^{-3}$ nm^{-2}) which are greater than that of pure Y_2O_3 (1.58×10^{-3} nm^{-2}). A decrease in crystallite size (as determined by the W-H method) inevitably results in an increase in dislocation density, which implies that the stacking fault may decline as a function of dislocation density [21]. Additionally, Ag doped Y_2O_3 (7.11×10^{-4}) have lower estimated strains (ε) than the pure Y_2O_3 (8.32×10^{-4}). From the calculated crystallite size, dislocation density (δ) is used to identify the amount of crystal defects in the synthesized sample [22].

Table 1 XRD parameters of pure Y_2O_3 and Ag doped Y_2O_3 nanoparticles

Sample	Williamsons Hall method		
	Average crystallite size D (nm)	Strain $\varepsilon \times 10^{-4}$	Dislocation density $\delta \times 10^{-3}$ nm^{-2}
Pure Y_2O_3	25.14	8.32	1.58
Ag doped Y_2O_3	16.21	7.11	3.81

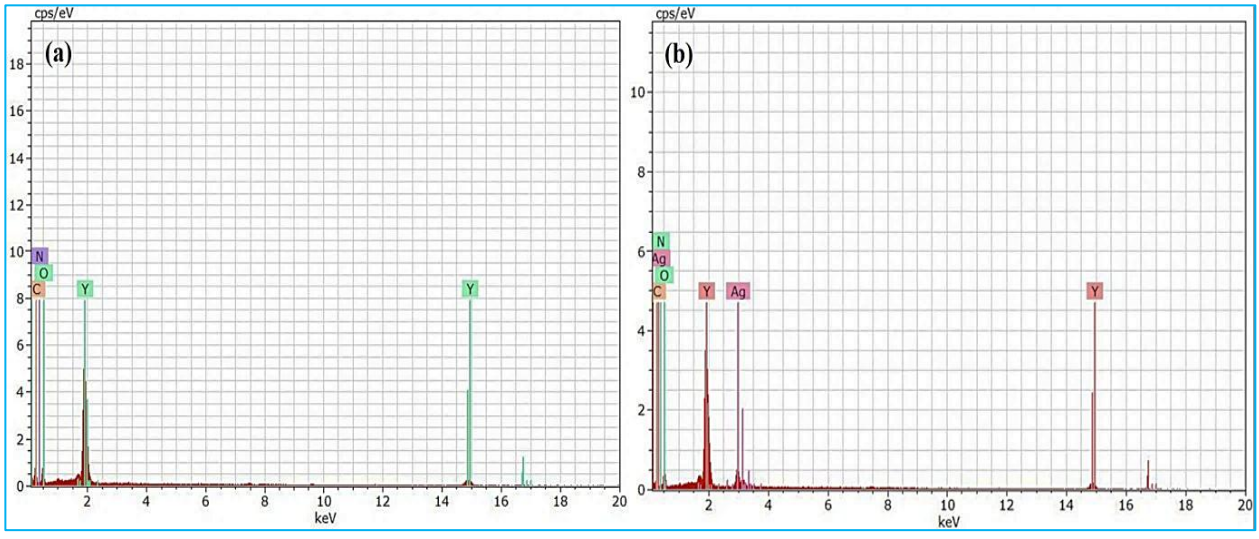

Fig 3 EDS spectra of (a) pure Y_2O_3 and (b) Ag doped Y_2O_3 nanoparticles

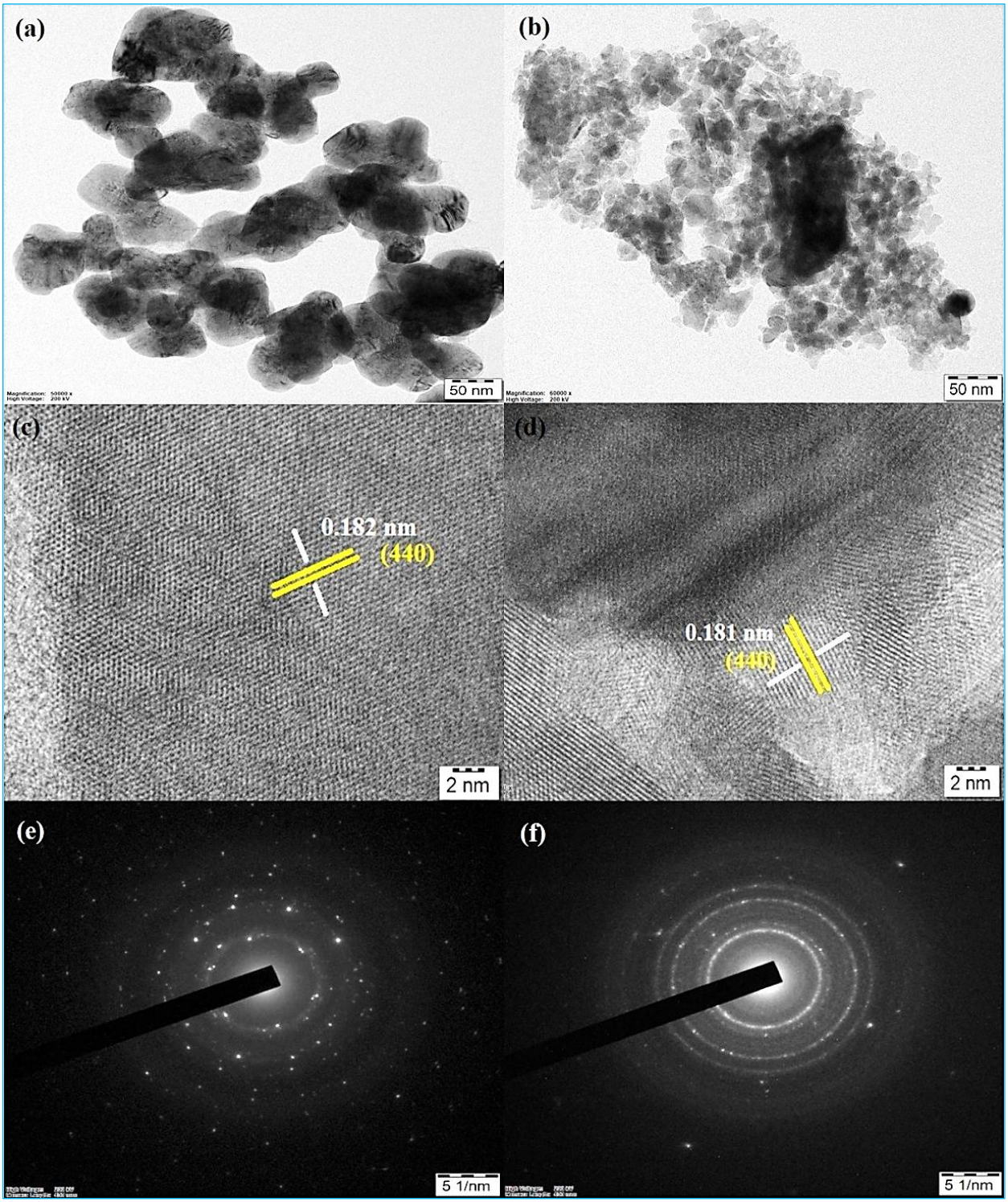

Fig 3 (a-b) TEM image, (c-d) HRTEM image and SAED (e-f) of pure Y_2O_3 and Ag doped Y_2O_3 nanoparticles

TEM and EDS analyses

As synthesized nano-powders were analyzed by Transmission Electron Microscopy (TEM) and presented in (Fig 3a-b). The pure Y_2O_3 and Ag doped Y_2O_3 nanoparticles appeared to be irregular and spherical shape. An average length and width of the Ag doped Y_2O_3 nanoparticles are determined to be 57.11 nm and 45.03 nm respectively. Higher magnification analysis (HRTEM) showed a lattice planar spacing of 0.182 nm for pure Y_2O_3 and 0.181 nm for Ag doped Y_2O_3 nanoparticles, which was in agreement with literature value for the (440) plane (Fig 3c-d) of 0.178 nm [23]. (Fig 3e-f) shows the SAED pattern of Y_2O_3 and Ag doped Y_2O_3 nanoparticles having diffraction rings with discrete diffraction spots, good agreement with the observed XRD results, which prove the face cantered cubic structure of Y_2O_3 nanoparticles. (Fig 3) shows the EDS spectrum of pure Y_2O_3 and Ag doped Y_2O_3 nanoparticles. From the EDS spectrum of pure Y_2O_3 (Fig 4a), the composition of yttrium (Y) and oxygen (O) peaks approves the purity of pure Y_2O_3 nanoparticles. From the (Fig 3b), the existence of silver (Ag) peak in Ag doped Co_3O_4 nanoparticles.

XPS spectra

X-ray photoelectron spectroscopy (XPS) measurements are carried out to analyze the surface element states and contents of pure Y_2O_3 and Ag doped Y_2O_3 nanoparticles. The full survey spectrum of Ag doped Y_2O_3 nanoparticles displays characteristics of C 1s, O 1s, Y 3d and Ag 3d (Fig 4), indicating the presence of these four elements, which is consistent with the EDS mapping results. Charge correction has been applied to all

the observed data of all elements with respect to C1s, which appears typically at 282.88 eV. The primary cause of C1s appearance during atmospheric exposure is adventitious carbon [24]. The XPS profiles of Co 2p are displayed for the quantitative analysis of surface elements in (Fig 5a), the prominent Y $3d_{5/2}$ and Y $3d_{3/2}$ peaks are located at 156.31 and 159.67 eV, respectively. The XPS spectrum of Y_2O_3 is highly consistent with those obtained in previous studies [25]. The agreement in both composition and binding energy proves the existence of Y_2O_3. Moreover, the O 1s spectrum is deconvoluted into three peaks (Fig 5b). The peak at the higher binding energy 532.02 eV is due to the oxygen vacancies on the surface of Ag doped Y_2O_3. The relatively low binding energy at 529.58 eV is attributed to lattice oxygen, which particularly demonstrates the existence of YO. The O^- and O^{2-} ions in the oxygen-deficient zone are brought on by the oxygen vacancies that are responsible for the higher binding energy species of O_2, which are cantered at 530.57 eV. The variation in peak intensity could be attributed to changes in the number and concentration of oxygen vacancies [26]. In the XPS spectrum of Ag 3d (Fig 5c), two peaks of Ag $3d_{5/2}$ (368.18 eV) and Ag $3d_{3/2}$ (374.26 eV) were correspond to metallic silver (Ag^0) and silver ions Ag^+, respectively, which agrees well with previous reports [27]. The XPS results also confirmed the successful synthesis of pure Y_2O_3 and Ag doped Y_2O_3 nanoparticles already demonstrated by EDX and XRD measurements.

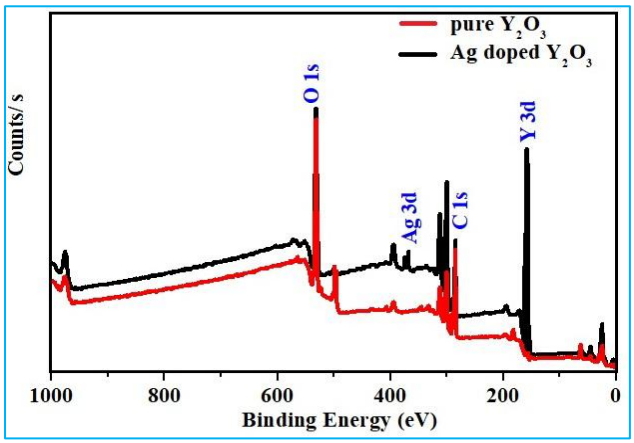

Fig 4 X-ray photoemission survey spectra of pure Y_2O_3 and Ag doped Y_2O_3 nanoparticles

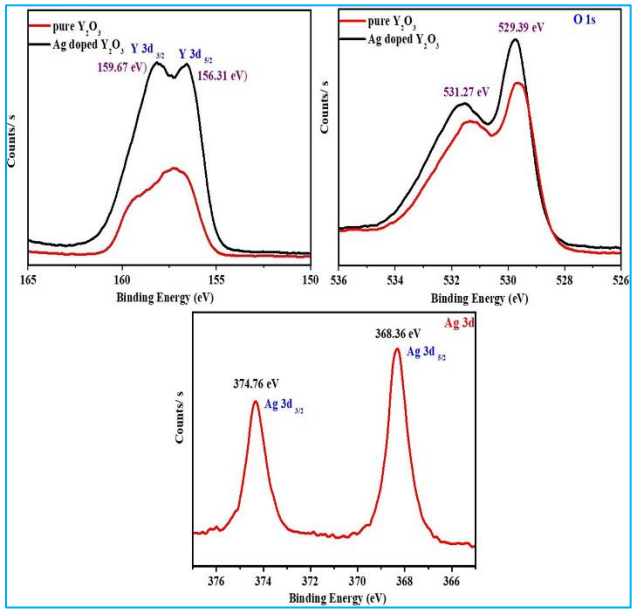

Fig 5 XPS spectrum of (a) Y 3d (b) O 1s and (c) Ag 3d

UV-visible spectra

The UV-visible absorption spectra of the pure Y_2O_3 and Ag doped Y_2O_3 nanoparticles as displayed in (Fig 6). The optical properties of nanostructures strongly depend on the absorbance of the material related to the transition of charges from the valence band to the conduction band [28]. The spectra show broad absorption, which is due to the creation of surface related defects in the nanoparicles [29]. Ali *et al*. [30] reported that the sharp absorption edge is characteristic of a homogeneous structure. The spectra show the absorption edge value of Ag doped Y_2O_3 nanoparticles was shifted to higher wavelength compared to Y_2O_3 nanoparticles, which confirmed the successful incorporation of Ag in Y_2O_3 lattice. From the absorbance spectra, the Ag doped Y_2O_3 nanoparticles do absorb strongly in the UV and visible portions. The pure Y_2O_3 does not absorb strongly in the visible region, where, the transmittance increases to around 100% or less.

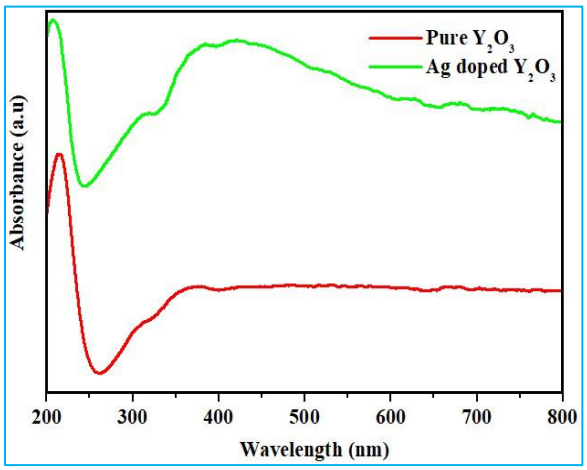

Fig 6 UV-visible absorbance spectra of pure Y_2O_3 and Ag doped Y_2O_3 nanoparticles

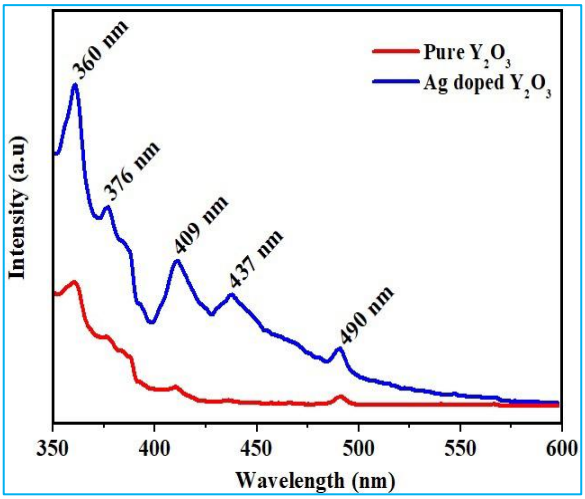

Fig 7 PL spectra of pure Y_2O_3 and Ag doped Y_2O_3 nanoparticles

PL spectra

The photoluminescence (PL) spectra of pure Y_2O_3 and Ag doped Y_2O_3 nanoparticles are measured at room temperature as shown in (Fig 7). The UV region (below 400 nm) accounts for the near band edge (NBE) emission while the deep level (DL) emissions are attributed for the visible region (above 400 nm) such that both the regions are accommodated well within the UV–visible luminescence bands [31]. Addition of dopant (Ag) the emission intensity compared to pure Y_2O_3 nanoparticles, which may happen due to the defects like single

ionized oxygen vacancy [32]. Increase the electron–hole recombination in valence band, increases the emission intensity of Ag doped Y_2O_3 nanoparticles. All the samples exhibit a broad UV emission band from 300 to 400 nm and three emission peaks in the visible regions. The strong UV emission band is divided into two peaks around 360 nm and 376 nm, which are attributed to the near band edge emission (NBE) free excitons in the conduction band [31]. Meantime, the violet emission at 405.11 nm is ascribed due to the existence of interstitial yttrium. The radiative recombination between the shallow donor (Y_i) and deep acceptor (V_o) levels would yield the observed violet emission around 409 nm [33]. The blue emission peak at 437 nm and 490 nm for both samples attributed to the defect-related emission or surface impurities (such as intrinsic defects, oxygen vacancies and surface state, and interstitial metal ions in the oxide) present in the cobalt oxide crystal occurred during growth [24].

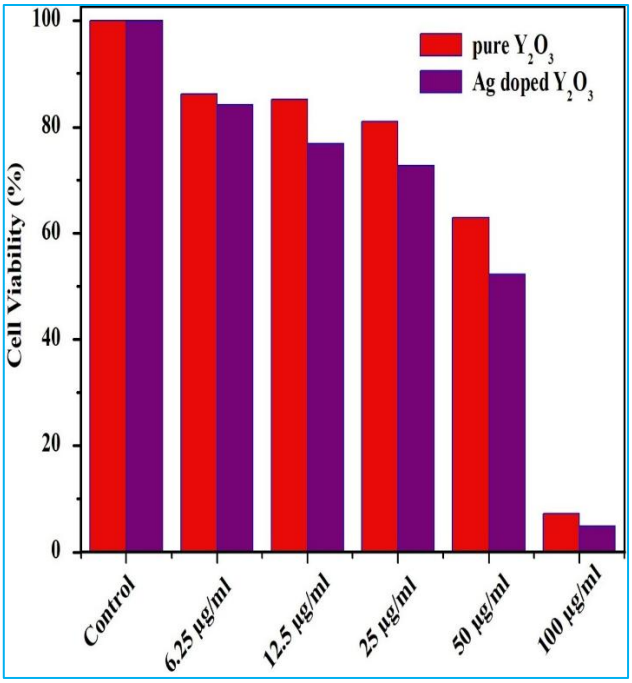

Fig 8 Percent cell viability values of AGS cells treated by different concentrations/ doses of pure Y_2O_3 and Ag doped Y_2O_3 nanoparticles after the incubation period of 24hrs by MTT assay

Anticancer activity

The viability of AGS (Human gastric adenocarcinoma) cell lines were studied to evaluate the anticancer potency of the green synthesized pure Y_2O_3 and Ag doped Y_2O_3 nanoparticles using different concentration/dose of nanostructures (i.e. 6.25–100 µg/ml) by MTT assay. (Fig 8) depicts the relative percent viability of the cancerous AGS cells. It has been observed that AGS cells viability is greatly inhibited by the prepared nanoparticles. Application of 100 µg/ml of the synthesized nanoparticle was resulted in better inhibition of AGS cells relative to the untreated cells. It was found that when the concentration of pure Y_2O_3 was increased from 6.25 µg /ml to 100 µg /ml, the cell viability progressively dropped from 85.11% to 7.23%, respectively. Nevertheless, it was possible to obtain that the cell viability gradually decreased from 84.09% to 4.92%, respectively, for an increase in Ag doped Y_2O_3 nanoparticles concentration from 6.25 µg/ml to 100 µg/ml. Hence, these cell viability results suggest that Ag doped Y_2O_3 nanoparticles possess higher anticancer activity as compared to pure Y_2O_3 nanoparticles. Cytotoxicity of the Y_2O_3 is generally linked with several factors such as particle size, ROS generation and release of metal ions [34]. Researchers have reported that Y_2O_3 nanoparticles have the potential to genotoxic effects, generate oxidative stress, cell death, DNA damage, cell death, and inflammatory responses [35]. Results showed that Ag doped Y_2O_3 nanoparticles induced intracellular ROS generation in a dose dependent manner. The results of Ag doped Y_2O_3 nanoparticles were showed that concentration/dose dependent study had reduced the cell viability of AGS cell lines. The Ag doped Y_2O_3 nanoparticles disturb the cell well and damages the cancer cell function. The efficacy of cobalt ions containing compounds on cancer cells has been ascribed to the ability of the ions to penetrate the cells where they produce reactive oxygen species (ROS) which are able to induce apoptosis in cancer cells [36]. Silver induces apoptosis in malignant cells by elevating the concentration of free radicals within them [37]. This shows that Ag doped Y_2O_3 nanoparticles can be a potential candidate with improved efficacy against cancerous cells. The role of the enhanced absorbance of metal-oxide nanoparticles in ROS mediated toxicity reported by Akhtar *et al*. [38]. The red shift of the absorption edge of Ag doped Y_2O_3 nanoparticles acting critical role in ROS mediated cytotoxicity. Moreover, we also perceived the superior cytotoxic influence of *Clerodendrum infortunatum* leaf extract meditated Ag doped nanoparticles than the pure ones and realized the impact of doped silver ion raising the rate of induced cytotoxicity.

The suggested MTT test for human AGS cells from pure Y_2O_3 and Ag doped Y_2O_3 nanoparticles are displayed in (Fig 9). As can be seen in the figure, the samples inhibited the growth of AGS cells using MTT staining, and as the concentrations/dose of 6.25 µg/ml, 12.5 µg/ml, 25 µg/ml, 50 µg/ml and 100 µg/ml were increased, the cell survival rates decreased in tandem. This image reveals a considerable amount of cell death after the prepared samples were treated [39]. For biomedical purposes, especially in vivo applications, toxicity is a critical factor to consider when evaluating their potential. Green synthesis nanoparticles for imaging and drug delivery are often purposely coated with bioconjugates such as DNA, proteins, and monoclonal anti small bodies to target specific cells. As these nanoparticles are intentionally engineered to interact with cells, it is important to ensure that these enhancements are not causing any ad verse effects. More significant is whether either naked or coated nanoparticles will undergo biodegradation in the cellular environment and what cellular responses degraded nanoparticles induce [40]. According to the MTT results, Ag doped Y_2O_3 nanoparticles had a greater probability than pure Y_2O_3 as a contributor to cell death. Therefore, the synthesis of Ag doped Y_2O_3 mediated through *Clerodendrum infortunatum* leaf extract demonstrates that these Ag doped could have chemotherapeutic effects which can be pioneered for the making of drugs.

CONCLUSION

In the present investigation, we report a simple, safe, environment friendly and economical biological technique for synthesizing Ag-doped Y_2O_3 nanoparticles with *Clerodendrum infortunatum* leaf extraction. The synthesized nanoparticles were characterized by various techniques, including XRD, TEM, XPS, UV-visible and PL. Our findings on anticancer activity demonstrated that Ag-doped Y_2O_3 nanoparticles induce cytotoxicity in AGS (Human gastric adenocarcinoma) cell lines, which is mediated by generation of ROS and oxidative stress. Therefore, it is envisaged that these Ag-doped Y_2O_3 nanoparticles may be exploited in drug delivery and pharmaceutical industry.

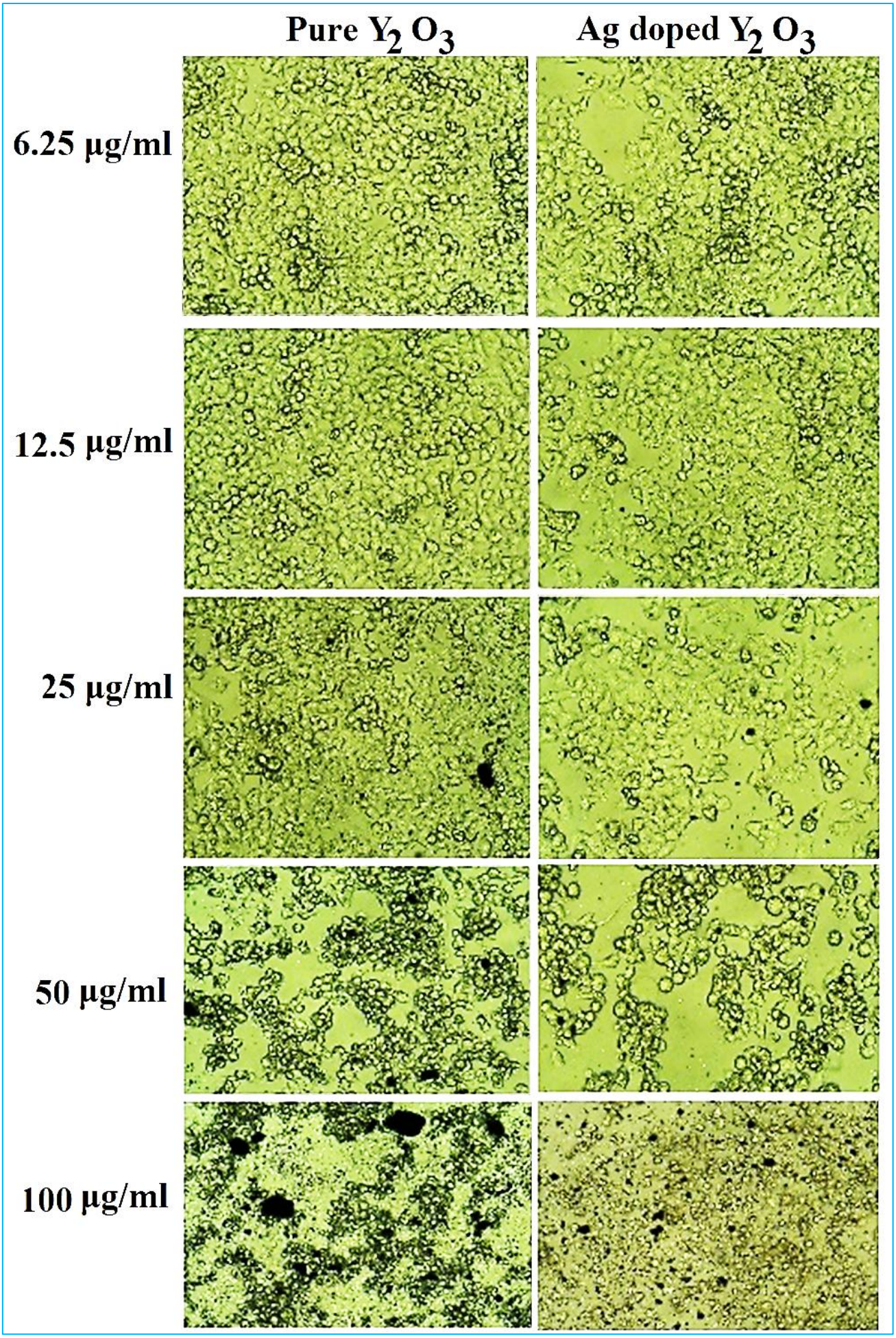

Fig 9 Cell numbers and viability evaluated using MTT staining after 24 h seeding
(6.25 µg/ml, 12.5 µg/ml, 25 µg/ml, 50 µg/ml and 100 µg/ml)

LITERATURE CITED

1. Ardalani S, Ahmadi R, Torabi P. 2022. The cytotoxic effects of green synthesized AgCl2 nanoparticles on gastric cancer (AGS) cells. *Journal of Biological Studies* 5: 1-9.
2. Tabaku M, Noroozi S, Ahmadi R. 2023. Tolectin in vitro effects on TRP53 gene expression level in gastric adenocarcinoma cells. *Journal of Biological Studies* 6: 125-138.
3. Herin RF, Judit ASS, Sebastiammal S, Shabna S, Dhas SSJ, Biju CS. 2024. Functionalized ZnO NPs and biopolymers-coated ZnO NPs for drug delivery and biomedical applications: A review. *Regenerative Engineering and Translational Medicine* 11(1): 165-189.
4. Venkatachalam V, Kumar VK, Selvi PK, Maske AO, Anbarasan V, Kumar PS. 2011. Antidiabetic activity of *Lantana camara* Linn fruits in normal and streptozotocin-induced diabetic rats. *Jr. Pharm. Research* 4: 1550-1552.
5. Garg SK, Shah MA, Garg KM, Farooqui MM, Sabir M. 1997. Antilymphocytic and immunosuppressive effects of *Lantana camara* leaves in rats. *Indian Jr. Exp. Biology* 35: 1315-1328.
6. Patil SP, Kumbhar ST. 2018. Evaluation of terpene-rich extract of *Lantana camara* L. leaves for antimicrobial activity against mycobacteria using Resazurin Microtiter Assay (REMA). *Beni-Suef Univ. Jr. Basic Applied Science* 7: 511-515.
7. Setua S, Menon D, Asok A, Nair S, Koyakutty M. 2010. Folate receptor targeted rare-earth oxide nanocrystals for bi-modal fluorescence and magnetic imaging of cancer cells. *Biomaterials* 31: 714-729.
8. Srinivasan R, Yogamalar NR, Elanchezhiyan J, Joseyphus JR, Bose CA. 2010. Structural and optical properties of europium doped yttrium oxide nanoparticles for phosphor applications. *Journal of Alloys and Compounds* 496: 472-477.
9. Yazgan Kokuoz B, Serivalsatit K, Kokuoz B, Geiculescu O, McCormick E, Ballato J. 2009. Er-Doped Y2O3 Nanoparticles: A comparison of different synthesis methods. *Journal of American Ceramic Society* 92: 2247-2253.
10. Phan TL, Chung DN, Thang PD, Huyen PT, Manh TV, Ho TA, Thanh TD, Vuong NM, Lee BW, Yu SC. 2015. Crystal structure and photoluminescence properties of Eu-Doped Y_2O_3 nanoparticles prepared by mechanical milling. *Materials Transactions* 56: 1412-1415.
11. Geitenbeek RG, Salzmann BBV, Nieuwelink AE, Meijerink A, Weckhuysen BM. 2019. Chemically and thermally stable lanthanide-doped Y_2O_3 nanoparticles for remote temperature sensing in catalytic environments. *Chemical Engineering Science* 198: 235-240.
12. Benammar I, Salhi R, Deschanvresc JL, Maalej R. 2020. The effect of rare earth element (Er, Yb) doping and heat treatment on suspension stability of Y_2O_3 nanoparticles elaborated by sol-gel method. *Journal of Materials Research Technology* 9: 12634-12642.
13. Pradhan SK, Pareek V, Panwar J, Gupta S. 2019. Synthesis and characterization of ecofriendly silver nanoparticles combined with yttrium oxide (Ag-Y_2O_3) nanocomposite with assorted adsorption capacity for Cu(II) and Cr(VI) removal: A mechanism perspective. *Journal of Water Process Engineering* 32: 100917-100931.
14. Ullah A, Saadullah M, Alvi F, Sherin L, Ali A, Shad NA, Javed Y, Sajid MM, Yasin G, Abbas W. 2022. Synergistic effect of silver doped ZnO nanomaterials enhances the anticancer potential against A459 lung cancer cells. *Journal of King Saud University – Science* 34: 101724.
15. Parveen K, Banse V, Ledwani L. 2016. Green synthesis of nanoparticles: Their advantages and disadvantages. *American Institute of Physics* 1724: 020048.
16. Ameen F. 2022. Optimization of the synthesis of fungus-mediated bi-metallic Ag-Cu nanoparticles. *Applied Science* 12: 1384.
17. Singh R, Dutta S. 2017. Synthesis and characterization of solar photoactive TiO_2 nanoparticles with enhanced structural and optical properties. *Advanved Powder Technology* 29: 211.
18. Kumar S, Bithel N, Kumar S, Kishan, Sen M, Banerjee C. 2024. Phyto-mediated synthesis of zinc oxide nanoparticles from *Clerodendrum infortunatum* L. leaf extract and evaluation of antibacterial potential. *South African Journal of Botany* 164: 146.
19. Pradhan SK, Pareek V, Panwar J, Gupta S. 2019. Synthesis and characterization of ecofriendly silver nanoparticles combined with yttrium oxide (Ag-Y_2O_3) nanocomposite with assorted adsorption capacity for Cu(II) and Cr(VI) removal: A mechanism perspective. *Journal of Water Process Engineering* 32: 100917-100932.
20. Samuel J, Shaji JE, Dhas SSJ, Suresh S, Vinita VS, Biju CS. 2023. UV-blocking performance and antibacterial activity of Cd, Ba co-doped ZnO nanomaterials prepared by a facile wet chemical method. *Surface and Interface Analysis* 55(4): 1-14.
21. Samuel J, Suresh S, Shabna S, Vinita VS, Ananth NJ, Shinu PMS, Mariappan A, Simon T, Samson Y, Biju CS. 2022. Characterization and antibacterial activity of Ti doped ZnO nanorods prepared by hydrazine assisted wet chemical route. *Physica E* 143: 115374-115385.
22. Yogamalar R, Srinivasan R, Vinu A, Ariga K, Bose AC. 2009. X-ray peak broadening analysis in ZnO nanoparticles. *Solid State Communication* 149: 1919.
23. Park CW, Park DJ. 2021. Development of Er3+, Yb3+ Co-Doped Y2O3 NPs According to Yb3+ Concentration by LP–PLA method: Potential further biosensor. *Biosensors* 11: 150-164.
24. Samuel J, Rajesh TSF, Biju CS, Dhas SSJ, Usharani S. 2023. Synthesis, structural, photoluminescence, ultraviolet blocking and antibacterial performances of Ba-doped ZnO nanostructures. *Results in Optics* 12: 100482-100489.
25. Liu M, Liu W, Liu X, Ouyang Y, Hou H, Lei M, Wei Z. 2020. Yttrium oxide as a Q-switcher for the near-infrared erbium-doped fiber laser. *Nanophotonics* 9: 2887-2894.
26. Singh CJC, Samuel J, Biju CS, Dhas SSJ, Usharani S. 2023. Effect of Sn doping on the structural, photoluminescence, ultraviolet filtering and antibacterial activity of ZnO nanorods. *Optical and Quantum Electronics* 55: 1072-1093.
27. Iqbal S, Javed M, Bahadur A, Qamar MA, Ahmad M, Shoaib M, Raheel M, Ahmad N, Akbar MB, Li H. 2020. Controlled synthesis of Ag-doped CuO nanoparticles as a core with poly (acrylic acid) microgel shell for efficient removal of methylene blue under visible light. *Journal of Materials Science: Materials in Electronics* 31: 8423-8432.
28. Fanga J, Xuan Y. 2017. Investigation of optical absorption and photothermal conversion characteristics of binary CuO/ZnO nanofluids. *RSC Advances* 7: 56023-56037.

29. Jia H, Zhang X, Feng Z, Cao Y. 2022. Y_2O_3:Eu@SiO_2 nanocomposites as a convertor for a broadband solar-blind UV photodetector. *Journal of the American Ceramic Society* 105: 5252-5267.
30. Ali AG, Dejene FB, Swart HC. 2017. Narrow visible emission and narrowing band gap in Ho3+ -Co Doped Y_2O_3: Eu3+ Nano-powders Prepared Via Sol- Combustion Routem. *IOSR Journal of Applied Physics* 9: 23-33.
31. Ravi A, Samuel J, Dhas SSJ, Usharani S, Simon T, Kumar DS, Vijitha SKJ, Sivakumar A, Kumar RS, Biju CS. 2014. Structural, morphological, optical and antibacterial performances of rare earth (Sm)-doped ZnO nanorods. *Journal of Rare Earths* 42(4): 1-9.
32. Huang H, Sun X, Wang S, Liu Y, Li X, Liu J, Kang Z, Lee ST. 2011. Strong red emission of pure Y_2O_3nanoparticles from oxygen related defects. *Dalton Transactions* 40: 11362-11366.
33. Pramothkumar A, Senthilkumar N, Gnana Malar KCM, Meena M, Potheher IV. 2019. A comparative analysis on the dye degradation efficiency of pure, Co, Ni and Mn-doped CuO nanoparticles. *Journal of Materials Science: Materials in Electronics* 30: 19043.
34. Jan T, Iqbal J, Farooq U, Gul A, Abbasi R, Ahmad I, Malik M. 2015. Structural, Raman and optical characteristics of Sn doped CuO nanostructures: A novel anticancer agent. *Ceramics International* 41: 13074.
35. Abudayyak M, Gurkaynak TA, Zhan G. 2017. In vitro evaluation of cobalt oxide nanoparticle-induced toxicity. *Toxicology and Industrial Health* 33: 646-654.
36. Prabhu S, Thangadurai TD, Bharathy PV. 2021. Green based biosynthesis of zinc oxide nanoparticles using *Clitoria ternatea* flower extract and its antibacterial activity. *Nano Biomedicine and Engineering* 13(4): 394-400.
37. Yazdi MET, Amiri MS, Akbari S, Sharifalhoseini M, Nourbakhsh F, Mashreghi M, Yousefi MRE, Abbasi M, Modarres AH. 2020. Green synthesis of silver nanoparticles using helichrysum graveolens for biomedical applications and wastewater treatment. *Bio. NanoScience* 10: 1121-1127.
38. Akhtar MJ, Alhadlaq HA, Alshamsan A, Khan MAM, Ahamed M. 2015. Aluminum doping tunes band gap energy level as well as oxidative stress-mediated cytotoxicity of ZnO nanoparticles in MCF-7 cells. *Scientific Reports* 5: 13876.
39. Ahamed M, Akhtar MJ, Khan MAM, Alhadlaq HA. 2022. Enhanced anticancer performance of eco-friendly-prepared MoZnO/RGO nanocomposites: Role of oxidative stress and apoptosis. *ACS Omega* 7: 7103.
40. Lewinski N, Colvin V, Drezek R. 2008. Cytotoxicity of nanoparticles. *Small* 4(1): 26-49.